This article has been accepted for publication in IEEE Access. This is the author's version which has not been fully edited and content may change prior to final publication. Citation information: DOI 10.1109/ACCESS.2026.3730400

Date of publication xxxx 00, 0000, date of current version xxxx 00, 0000.

Digital Object Identifier

Grounding Analysis of Noncontact Three-Phase Voltage Measurement

THOMAS C. KRAUSE[1], AARON W. LANGHAM[2], DAISY H. GREEN [3], AND STEVEN B. LEEB[4]
[1]Elmore Family School of Electrical and Computer Engineering, Purdue University, West Lafayette, IN 47906 USA
[2]The Cooper Union for the Advancement of Science and Art, New York, NY 10008 USA
[3] Department of Electrical and Computer Engineering, University of Hawai'i at Manoa, Honolulu, HI 96822 USA
[4]Department of Electrical Engineering and Computer Science, Massachusetts Institute of Technology, Cambridge, MA 02139 USA

Corresponding author: Thomas C. Krause (e-mail: krause24@purdue.edu).

This work is supported by the Office of Naval Research under contract N00014-23-1-2728 and additional funding from the Electric Ship Research and Development Consortium and The Landsman Foundation.

ABSTRACT This paper analyzes how power system grounding impacts capacitive noncontact three-phase ac voltage measurement of multi-wire cables. Experimental results with new sensing hardware verify the analysis. Contributions of this work include guidelines and conditions for successful sensing in a variety of grids, including ungrounded, high-resistance grounded, and solidly grounded three-phase power systems.

INDEX TERMS Capacitive sensors, power monitoring, voltage measurement, power system grounding.

I. INTRODUCTION

POWER monitoring with a non-intrusive load monitor (NILM) offers valuable services for critical energy systems including load identification, energy scorekeeping, and equipment fault detection and diagnostics [1]. Typical NILM installations use voltage sensors that require galvanic contact with conductors and current sensors that require rewiring bus conductors in an electrical panel. In contrast, noncontact sensors measure voltages and currents with less installation effort. They enable monitoring of previously inaccessible grids and unlock potential economic benefits to equipment operators [2]–[4]. For widespread adoption, noncontact sensing techniques must accommodate a variety of power system scenarios and topologies. For example, three-phase ac power systems may employ different ‘‘grounding" methods, ranging from solidly grounded distribution systems in buildings to ungrounded microgrids on ships [5]–[8]. This paper investigates how power system grounding impacts voltage sensing circuits and signal processing of an electrode-array noncontact power meter for multi-wire cables.

As a step towards a self-calibrating, fully noncontact power meter, publication [9] presented a new electrode-array noncontact voltage sensor for multi-wire cables. This self-calibrating sensor design features a sensing probe which wraps around the outside of a power cable, in contrast to ‘‘open-air’’ noncontact voltage sensing for overhead lines [10]–[12]. Capacitive coupling between an array of sensing electrodes on the probe and the internal cable wires enables sensing and ac voltage waveform reconstruction. Reference [9] introduced the sensing approach and detailed three methods to estimate electrode-to-wire coupling capacitances via an injected signal. Tests with a hardware prototype installed on a three-phase power cable of a solidly grounded power system characterized capacitance estimation and voltage reconstruction performance. While previous analysis and tests were limited to solidly grounded systems, this paper expands the ideas in [9] and analyzes capacitive noncontact voltage sensing in three-phase ac grids with arbitrary grounding circuits. This includes ungrounded, high-resistance grounded, or solidly grounded power systems. Contributions of this paper include circuit models for the power system and sensor, circuit analysis, and conditions that explain when this style of sensor can or cannot reliably self-calibrate or reconstruct system voltages. Additionally, this paper introduces new sensing hardware, featuring a multiplexed analog front end, which experimentally verifies the modeling and analysis. Analyses apply generally and experiments focus on sensor performance in the strictest scenario, ungrounded power systems, like those found in shipboard microgrids. The analysis and experimental results demonstrate that noncontact three-phase voltage sensors can perform in essentially all practical power system configurations.

Section II of this paper reviews the electrode-array noncontact voltage sensor and presents new hardware that facilitates experimental results. Section III analyzes sensor operation. Section IV presents experimental results which validate circuit analysis.

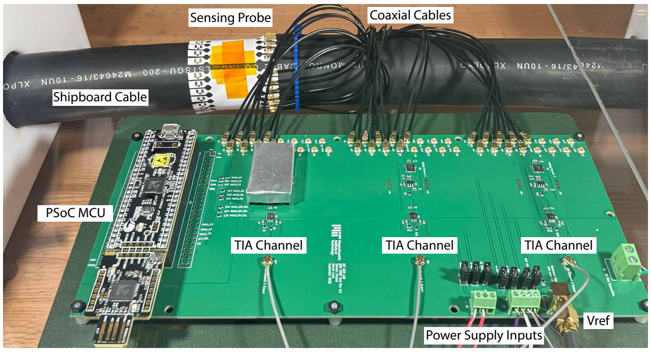

FIGURE 1. Laboratory setup of electrode-array noncontact voltage sensor prototype installed on a LSTSGU-200 three-phase three-wire cable. This prototype features three TIA channels with multiplexed inputs. A shield covers one TIA channel and the others are exposed to display circuitry.

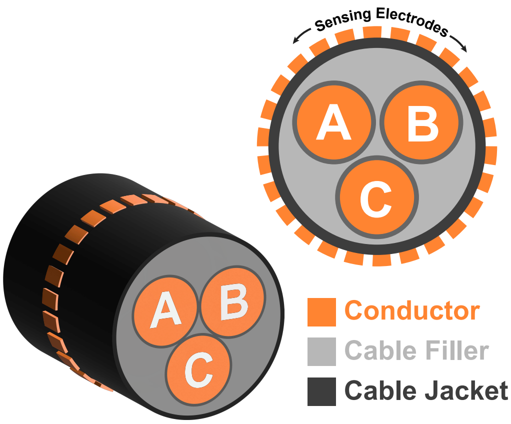

FIGURE 2. Cross-section diagram of flexible PCB sensing electrodes and three-wire three-phase power cable [9].

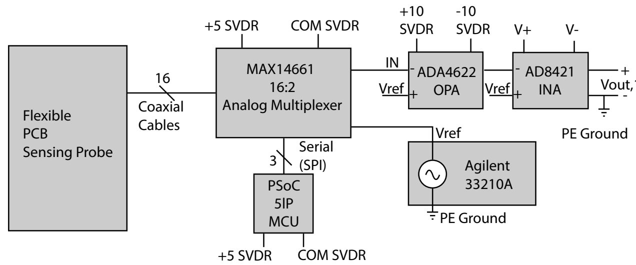

FIGURE 3. Block diagram of one of the TIA channels in Fig. 1 with 16:2 multiplexer and SVDR technique.

II. NONCONTACT VOLTAGE SENSOR SYSTEM

This section presents noncontact voltage sensor instrumentation. Two main components comprise the sensor prototype, a flexible printed circuit board (PCB) sensing probe and a new transimpedance amplifier (TIA) board which employs analog multiplexers and a supply voltage driving (SVDR) technique. These circuits implement the driven electrode method for noncontact three-phase voltage measurement as described in [9]. This sensing method first injects an ac reference voltage onto sensing electrodes to identify coupling capacitances between electrodes and power system phase wires. Then, estimated capacitance values are used to relate sensed capacitive currents from TIAs to system voltages. Reference [13] describes relevant uncertainty analysis of the driven electrode method and TIA circuitry in a single-phase application. This section sets the stage for Sections III and IV, which analyze and demonstrate the performance of this sensor applied to three-phase grids with various grounding methods.

Fig. 1 shows the electrode-array noncontact voltage sensor installed on a section of LSTSGU-200 shipboard three-phase three-wire power cable. This setup uses the same 26-electrode flexible PCB sensing probe with rectangular 4.318 mm wide by 25.4 mm long electrodes as [9] but installed at a different location along the cable. Other sensing probe geometries with, for example, different electrode counts, multiple rows of electrodes, or skewed electrodes could provide performance benefits in certain applications depending on the target cable. Detailed optimization of the sensing probe and its electrodes presents is outside of the scope of this work. Polyimide tape secures the probe to the outer jacket of the cable. The sensing methods tolerate and correct for the gap between probe ends due to any slight mismatch between the probe length and cable circumference. Fig. 2 shows a conceptual cross-section view of the cable and sensing electrode system. The sensing electrodes sit approximately uniformly distributed around the cable circumference [9]. Every sensing electrode capacitively couples to every wire in the cable. The coupling capacitor values depend on the relative positions between and the size of conductors. To prevent unwanted coupling to other nearby wires, a shield conductor (not shown in Fig. 2) covers the top (outer) layer of the flexible PCB and shields the sensing electrodes present on the bottom (inner) layer.

The TIA board in Fig. 1 has three TIA channels, each with a MAX14661 16:2 analog multiplexer between the sensing probe connections and the TIA ADA4622-1 operational amplifier (OPA). A power supply setup with the SVDR technique of [14], [15] enables a multiplexed analog front end. The SVDR technique mitigates the effect of parasitic capacitance introduced by the multiplexer and inherent to the TIA op amp inverting terminal. It eliminates the need for digital estimation and subtraction of parasitic capacitance, which suffers from drifting capacitance values [13], [15]. Fig. 3 shows a block diagram of TIA channel 1. Up to 16 coaxial cables connect the sensing probe electrodes and MAX14661 analog multiplexer inputs via U.FL connectors. An equal number of consecutive sensing electrodes distributed to each multiplexer maximizes the chance that the closest electrode to each wire connects to a unique TIA channel. The outer conductors of the coaxial cables shield the inner conductors and help prevent capacitive coupling between the sensing electrodes and external conductors. A PSoC 5LP microcontroller (MCU), connected to a personal computer via a USB isolator, communicates via serial peripheral interface (SPI) to each

This article has been accepted for publication in IEEE Access. This is the author's version which has not been fully edited and content may change prior to final publication. Citation information: DOI 10.1109/ACCESS.2026.3730400

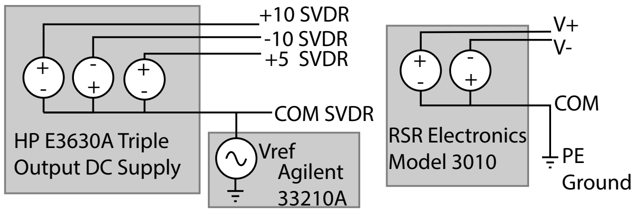

FIGURE 4. **Power supplies for SVDR technique.**

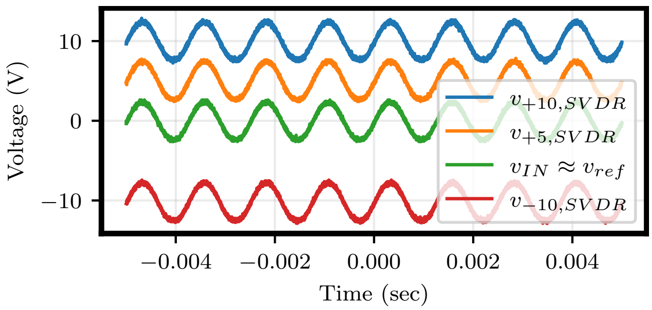

(a) Measured SVDR power supply ouput voltages and TIA inverting-input voltage with respect to PE ground.

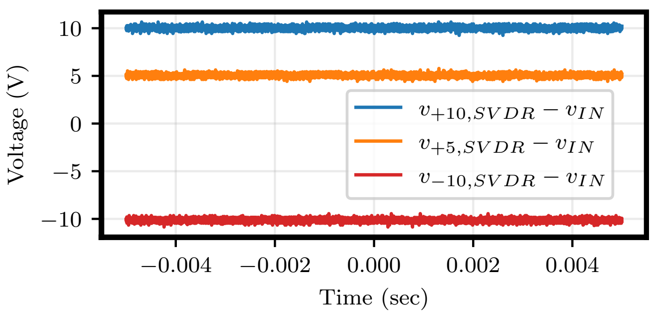

(b) Voltage differences between SVDR power rails and TIA inverting input.

FIGURE 5. **Measured SVDR technique signals.**

multiplexer and manages their connections. Internal switches connect each multiplexer input to one of two MAX14661 multiplexer outputs. In Fig. 3, the first output connects to the TIA input (ADA4622-1 inverting input terminal) and the second output connects to the ac reference voltage signal V_{ref}. During sensor operation, only one sensing electrode connects to the TIA. All other sensing electrodes connect the second multiplexer output and the reference voltage signal drives the electrodes to a well-defined voltage. If the board used a 16:1 analog multiplexer, any "unselected" sensing electrodes would be left floating and could cause unwanted coupling.

Fig. 4 shows a diagram of the signal generator and power supply setup for the SVDR technique. A function generator (Agilent 33210A) with its output referenced to protective earth (PE) ground[1] creates the ac reference voltage signal V_{ref}. This signal serves two main roles: excitation for coupling capacitance estimation and as the common potential for the front-end power supply. The signal V_{ref} also drives shield conductors like the outside of coaxial cables. The front-end supply (HP E3630A) creates three dc voltage outputs with respect to the voltage on its common (COM) terminal. To implement the SVDR technique, V_{ref} drives the COM terminal, therefore, measured with respect to PE ground, each output of the E3630A has V_{ref} superimposed on its nominal dc voltage. With respect to COM, i.e., V_{ref}, or any other E3630A output, the voltages are just dc. Fig. 5 demonstrates the SVDR technique with measurements from the SVDR circuits. The signals in Figure 5a with dc offsets are E3630A outputs with voltage setpoints of +10 V, +5 V, and −10 V and a 2.5 V amplitude, 800 Hz V_{ref} at the COM terminal. The signal centered around zero is the measured voltage of the TIA input, V_{IN}, which is driven to V_{ref} via negative feedback. All signals in Fig. 5a vary sinusoidally at 800 Hz with V_{ref}. Figure 5b shows the results of sample-by-sample subtraction of the power-rail measurements with the inverting input voltage. The E3630A outputs with respect to V_{IN} or V_{ref} simply take their commanded dc values.

The ±10 V rails from the E3630A power the TIA op amps and the +5 V and COM (V_{ref}) rails power the analog multiplexers and supervisory MCU. Arranged in this way and as demonstrated by Fig. 5, there is no ac voltage difference between nearby, onboard conductors and the TIA input. Thus, ideally, the TIA sources no current to stray capacitances across these nodes and all reference-frequency TIA current is related to capacitive coupling with the phase wires inside the target cable [15]. Lastly, a second split-rail power supply (RSR Electronics 3010) creates outputs referenced with respect to PE ground. These supplies power the AD8421 instrumentation amplifier (INA) of the TIA, which creates an output voltage compatible with PE ground-referenced measurement instruments such as an oscilloscope.

This sensor hardware is the first demonstration of a multiplexed TIA circuit for multiwire voltage measurement. The SVDR technique facilitates the use of analog multiplexers in the signal chain, whose stray capacitance to ground would normally prohibit their use in a circuit like this. Compared to an individual TIA circuit for each sensing electrode, the multiplexers significantly decrease the size and cost of the TIA PCB. For example the 26-electrode sensing probe in Fig. 1 requires 26 TIA channels without multiplexers, but only 3 channels with multiplexers. The specific realization described in this section demonstrates the sensing method, but many aspects of the hardware could be integrated together and optimized into single PCB or chip solutions.

The SVDR technique and multiplexed front end also present some challenges. For example, the SVDR technique requires multiple isolated power supplies. The multiplexed design measures a smaller set of signals compared to simultaneously measuring every sensing-electrode signal with a dedicated TIA. This creates a trade off between hardware cost and any noise-immunity or redundancy benefits from many TIA

[1]PE ground refers to the node or conductor to which metallic equipment cases are bonded. This node may be connected to earth through a ground rod or to the chassis/hull of a vehicle.

measurements and overconstrained, least-squares signal processing [9]. The combination of analog and digital sections in the multiplexer integrated circuit can create crosstalk interference. Accordingly, TIA circuits may require additional filtering to eliminate unwanted high-frequency contributions from digital lines internal to the multiplexer. For the hardware setup of this paper, additional single-pole low-pass filters at the output of the INAs in Fig. 1 with $\tau = (13\ \mathrm{k\Omega})(1\ \mathrm{nF})$ filter the TIA outputs before oscilloscope sampling to reduce signal components from crosstalk.

III. CIRCUIT ANALYSIS

Requirements for personnel safety, maintainability, and reliability determine power system grounding strategy. Broadly, grounding methods differ in their wiring and how they respond to faults between nominally current-carrying conductors and PE ground. For example, systems that prioritize continuity of service may employ an ungrounded design which tolerates one line-to-ground fault. Systems that prioritize fault detection may employ a solidly grounded design, which generates higher line-to-ground fault current for immediate detection by short-circuit protection devices [8].

Ideally, a three-phase noncontact voltage sensor would accurately reconstruct system voltages regardless of the system grounding. However, sensor self-calibration and measurement rely on high-impedance coupling, small currents, and unconventional conduction paths, which all complicate analysis. From [9], it is clear that ground-reference noncontact sensing works on solidly grounded grids with well-defined phase-to-ground potentials. However, ground-referenced sensing on ungrounded systems appears to create a contradiction. This section resolves this with circuit analyses that explain the effect of three-phase power system topology on noncontact voltage sensing. Section III-A presents a circuit model generally applicable to a variety of power system grounding strategies. Sections III-B and III-C incorporate the model and equations of Section III-A into analysis of the TIA circuitry considering reference signal and grid sources, respectively. Superposition of these analyses forms the complete circuit solution.

A. POWER SYSTEM AND TIA CIRCUIT MODEL

Figure 6 presents a general circuit model which describes the grounding circuits of a three-phase power system. The line-to-neutral voltage sources V_{an}, V_{bn}, and V_{cn} model the output of power system source equipment. The connections in Figure 6 match wye-connected generators and transformers. When modeling delta-connected equipment, the delta-wye transform relates equipment terminal voltages to V_{an}, V_{bn}, and V_{cn} and the neutral point n is fictitious. The impedances Z_{ag}, Z_{bg}, and Z_{cg} represent the lumped phase-to-ground impedance on each phase. These impedances typically model the unintentional capacitive coupling between the phase conductors and PE ground and the line-to-ground capacitance of EMI filters [8].

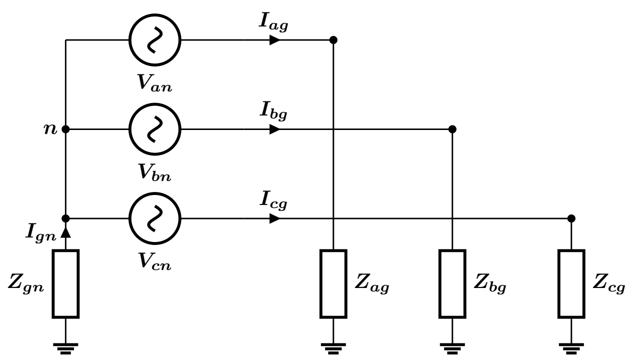

FIGURE 6. Lumped circuit model of the system voltages and grounding impedances associated with a three-phase ac power system.

In Fig. 6, the impedance Z_{gn} represents any impedance between PE ground and the source neutral point, if present. With proper choice of Z_{gn}, Fig. 6 can model all power system grounding strategies. Solidly grounded systems bond the neutral point to PE ground, making Z_{gn} a small-valued resistor or short circuit. High-resistance grounded power systems connect the neutral point to PE ground through a high-valued resistor. In that case, the model would include a moderately large and dominantly resistive Z_{gn}. Ungrounded systems with wye-connected transformers and generators leave the neutral point floating. Thus, Z_{gn} will be large and dominantly capacitive. Ungrounded systems with delta-connected sources have no neutral point. In analysis of ungrounded systems, Z_{gn} is an open circuit.

Circuit analysis of Fig. 6 starts with application of Kirchhoff's current law at the ground node, in the Laplace domain:

$$I_{ag}(s) + I_{bg}(s) + I_{cg}(s) = I_{gn}(s). \tag{1}$$

If Z_{gn} is an open circuit, $I_{gn}(s) = 0$ and all phase currents sum to zero. Otherwise, current flows through Z_{gn}, and by Ohm's Law, the ground-to-neutral voltage is

$$V_{gn}(s) = I_{gn}(s)Z_{gn}(s). \tag{2}$$

Ohm's Law also provides expressions for the line-to-ground currents,

$$I_{ag}(s) = \frac{V_{an}(s) - V_{gn}(s)}{Z_{ag}(s)} \tag{3}$$

$$I_{bg}(s) = \frac{V_{bn}(s) - V_{gn}(s)}{Z_{bg}(s)} \tag{4}$$

$$I_{cg}(s) = \frac{V_{cn}(s) - V_{gn}(s)}{Z_{cg}(s)}. \tag{5}$$

Substitution of Equations (3)-(5) into (2) yields

$$\frac{V_{an}(s) - V_{gn}(s)}{Z_{ag}(s)} + \frac{V_{bn}(s) - V_{gn}(s)}{Z_{bg}(s)} + \frac{V_{cn}(s) - V_{gn}(s)}{Z_{cg}(s)} = \frac{V_{gn}(s)}{Z_{gn}(s)}. \tag{6}$$

This article has been accepted for publication in IEEE Access. This is the author's version which has not been fully edited and
content may change prior to final publication. Citation information: DOI 10.1109/ACCESS.2026.3730400

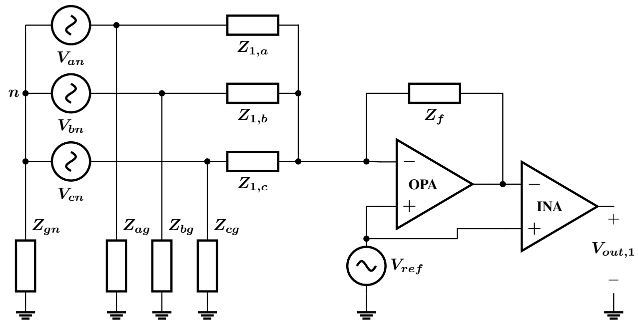

FIGURE 7. TIA sensing channel 1 of an *M* channel sensor coupled to a three-phase power system and with sensing circuitry referenced to PE ground.

Rearranging (6) and solving for $V_{gn}(s)$ gives its expression for an arbitrarily grounded three-phase system

$$V_{gn}(s) = \frac{\frac{V_{an}(s)}{Z_{ag}(s)} + \frac{V_{bn}(s)}{Z_{bg}(s)} + \frac{V_{cn}(s)}{Z_{cg}(s)}}{\frac{1}{Z_{ag}(s)} + \frac{1}{Z_{bg}(s)} + \frac{1}{Z_{cg}(s)} + \frac{1}{Z_{gn}(s)}}. \tag{7}$$

Millman's Theorem or the parallel generator theorem provides an alternative derivation of (7) [16]–[19]. Equation (7) evaluates to different values depending on the system grounding strategy. Specifically, consider the two limiting cases of solidly grounded, $|Z_{gn}| \rightarrow 0$, and ungrounded, $|Z_{gn}| \rightarrow \infty$. For a solidly grounded system, the ground-to-neutral voltage tends towards zero ($V_{gn}(s) \rightarrow 0$). For an ungrounded system, the ground-to-neutral voltage tends towards the expression

$$V_{gn}(s) = \frac{\frac{V_{an}(s)}{Z_{ag}(s)} + \frac{V_{bn}(s)}{Z_{bg}(s)} + \frac{V_{cn}(s)}{Z_{cg}(s)}}{\frac{1}{Z_{ag}(s)} + \frac{1}{Z_{bg}(s)} + \frac{1}{Z_{cg}(s)}}. \tag{8}$$

Equation (8) is exactly the voltage difference between the floating neutral point of a wye-connected load relative the neutral point of a wye-connected source (see Section III example (c) in [16]).

Combining the power system model with a sensor model describes TIA operation of a voltage sensor with sensing probe installed around a three-wire power cable. Fig. 7 shows the resulting circuit diagram for TIA channel 1 of an M channel voltage sensor. There are four voltage sources, three from the grid (V_{an}, V_{bn}, V_{cn}), and one from the sensor system (V_{ref}). Impedances $Z_{1,a}$, $Z_{1,b}$, and $Z_{1,c}$ represent the predominantly capacitive electrode-to-wire coupling impedances from electrode 1 to each of the phases of the power system. Other components comprise the TIA analog circuits discussed in Section II including the TIA OPA, TIA feedback network (Z_f), and TIA INA. For readability, Figure 7 does not show every circuit component of a sensor installation. It does not show the other $M-1$ TIA channels of the sensor which couple to the phases via different sets of impedances. Due to the SVDR technique of the prototype in Section II, it neglects parasitic input capacitance between the TIA inverting terminal and nearby nodes. Also, Fig. 7 omits the shield conductors, for example, the top layer of a two-layer flexible PCB sensing probe, outer conductors of the coaxial cables, or enclosures for TIA circuitry. These shield conductors directly connect to V_{ref} and have significant capacitance to the TIA inverting terminal and the power system phases. When relevant, other sections reintroduce any omitted components into equations and figures.

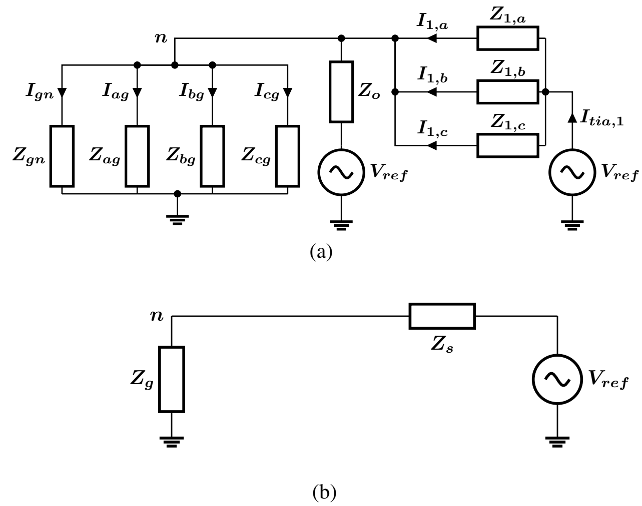

FIGURE 8. Reference-source equivalent circuits of TIA channel 1 of an *M* channel sensor.

B. REFERENCE-SOURCE ANALYSIS

After installation, the sensor self-calibrates and uses the reference signal component of the TIA output to identify the elements of the capacitance matrix [9]. Any uncertainty added to the reference signal outputs from power system grounding circuits directly degrades sensor performance. This section considers the reference signal voltage source of Fig. 7 and derives the impact of system topology on the self-calibration procedure of an M-channel noncontact voltage sensor. A contribution of this section is an impedance relationship that, if met, guarantees that system grounding circuits will not appreciably bias reference-signal measurements.

Assuming the inverting and non-inverting terminals of the TIA are virtually shorted, and turning off the grid voltage sources, simplifies Fig. 7 to the reference-source equivalent circuit in Fig. 8a. Note that because of the superposition analysis operations, the phase voltage nodes collapse into the neutral-point node labeled n. The V_{ref} source on the right represents the inverting input of the TIA op amp. The current through this source branch is the reference signal component of $I_{tia,1}$. The V_{ref} source in the middle represents any reference signal sources not from the TIA under consideration. This includes the "original" V_{ref}, e.g., the Agilent 33210A in Fig. 4, and the inverting terminals of other TIA channels. The impedance Z_o represents coupling between the phase conductors and these other V_{ref} sources, including shield-to-wire and electrode-to-wire capacitances. The output of the TIA from the reference signal source is

$$V_{out,1}(s) = -G_{tia}(s) I_{tia,1}(s) \tag{9}$$

where G_{tia} is the total gain in ohms of the TIA channel and may be frequency dependent, i.e., $G_{tia}(s) = G_{ina}Z_f(s)$, where G_{ina} is the gain of the instrumentation amplifier.

Due to the virtual short, the TIA input appears as a separate yet identical source to the original V_{ref} attached to its non-inverting terminal. The voltages of these sources are equal and circuit theory permits their combination. Once combined, Z_o connects in parallel with $Z_{1,a}$, $Z_{1,b}$, and $Z_{1,c}$. The combined V_{ref} source sees the series combination of two groups of parallel impedances. From right to left, the first impedance is the aggregate coupling between V_{ref} sources on the sensor and the phase conductors,

$$Z_s = Z_{1,a}||Z_{1,b}||Z_{1,c}||Z_o, \tag{10}$$

where $||$ represents a parallel connection between impedances. The second impedance is the aggregate coupling between the phase conductors and PE ground,

$$Z_g = Z_{gn}||Z_{ag}||Z_{bg}||Z_{cg}. \tag{11}$$

Fig. 8b shows the reduced version of Fig. 8a after these simplifications. Impedances Z_s and Z_g form a voltage divider which determines the voltage at node n,

$$V_n(s) = V_{ref}(s)\left(\frac{Z_g(s)}{Z_s(s) + Z_g(s)}\right) \tag{12}$$

and, by Ohm's law, the TIA current is

$$I_{tia,1}(s) = \frac{V_{ref}(s) - V_n(s)}{Z_{1,a}(s)||Z_{1,b}(s)||Z_{1,c}(s)}. \tag{13}$$

For purely capacitive electrode-to-wire coupling,

$$I_{tia,1}(s) = (V_{ref}(s) - V_n(s))\, s\,(C_{1,a} + C_{1,b} + C_{1,c})\,. \tag{14}$$

Sensor calibration relies on the magnitude of the TIA output at the reference frequency signal, $|V_{out,1}(j\omega_{ref})| = |G_{tia}(j\omega_{ref})I_{tia,1}(j\omega_{ref})|$, divided by the known TIA channel gain and V_{ref} magnitude for measurement of $C_{sum,1} = C_{1,a} + C_{1,b} + C_{1c}$ [9]. Illustrated by (14), this works when $V_n \approx 0$. Otherwise, the nonzero V_n diminishes $I_{tia,1}$ and causes inaccurate capacitance estimation.

Capacitance estimation without characterization of elements in Z_g requires that for every TIA channel

$$|Z_g(s)| << |Z_s(s) + Z_g(s)|. \tag{15}$$

Sensor capacitances on the order of 1-100 pF typically make up Z_s [9]. Solidly grounded power systems easily satisfy (15) because a direct electrical connection constrains $Z_{gn}(s) \approx 0$. Many ungrounded power systems will also satisfy (15), where capacitances from cable runs, Y capacitors in EMI filters, or other equipment form the elements of Z_g and exhibit values on the order of 0.1-1 µF [8]. However, there could be situations where (15) is not satisfied. In these cases, Z_g is too large relative to Z_s and a significant V_n attenuates $I_{tia,1}$ relative to the solidly-grounded case. Therefore, to avoid intrusive characterization of the quantities in (12), some action must decrease the magnitude of Z_g. One potential strategy adds grounded metallic structures near phase wires, e.g., tape or foil wrapped around the outside of the power cable and connected to PE ground, increasing phase wire capacitive coupling to PE ground and decreasing Z_g enough to satisfy (15). Analytical field approximations or finite-element electromagnetic solvers could estimate the additional capacitance added to Z_g by a foil wrap. Then, combined with knowledge of approximate values of Z_s from probe and cable geometry, the user could compute an estimate of (15). For an empirical approach, the user could observe the reference signal component of the sensor output as mitigation strategies decrease Z_g. The user would continue decreasing Z_g until the sensor output component no longer appreciably increases, indicating (15) is satisfied. However, this situation represents a worst case and required alteration of Z_g seems unlikely given the impedance magnitudes of typical sensors and power systems. Section IV-C experimentally verifies these results.

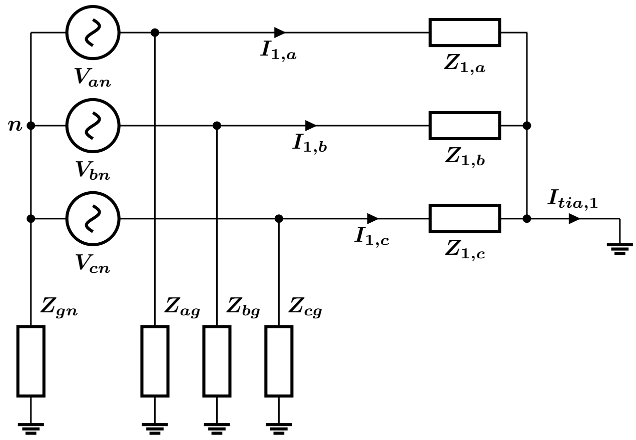

FIGURE 9. Grid-source equivalent circuit of TIA channel 1 of an *M*-channel sensor.

C. GRID-SOURCE ANALYSIS

After calibration with the reference signal, the sensor enters measurement mode. It uses capacitance estimates from the self-calibration procedure to reconstruct grid voltage waveforms. In measurement mode, the reference signal source is either turned off or its contributions filtered out of voltage estimates. This section considers the grid voltage sources of Fig. 7 and derives the impact of system topology on the grid-voltage estimates of an M-channel noncontact voltage sensor.

Assuming a virtual short and turning off V_{ref} forms the equivalent circuit in Figure 9. Kirchhoff's current law at the op amp inverting terminal yields

$$I_{tia,1}(s) = I_{1,a}(s) + I_{1,b}(s) + I_{1,c}(s), \tag{16}$$

where $I_{tia,1}(s) = I_{Z_f}(s)$ is the current through $Z_f(s)$ and $I_{1,a}(s)$, $I_{1,b}(s)$, and $I_{1,c}(s)$ are the currents through the coupling impedances between sensing electrode 1 and phases a, b, and c. The grid-source component of the output is

$$\begin{aligned} V_{out,1}(s) &= G_{tia}(s) I_{tia,1}(s) \\ &= G_{tia}(s)\left(I_{1,a}(s) + I_{1,b}(s) + I_{1,c}(s)\right). \end{aligned} \tag{17}$$

The sign in (17) is opposite from (9) because of the flipped $I_{tia,1}$ sign conventions in Fig. 8a and Fig. 9.

All sensor circuits, even SVDR power rails, ultimately connect to PE ground and use it as their global reference node. As explained in Section III-A, the PE ground has a voltage difference $V_{gn}(s)$ with respect to the source neutral point. Therefore, in the grid-source equivalent circuit, the grid-source currents through the electrode-to-wire coupling impedances are

$$I_{1,a}(s) = \frac{V_{an}(s) - V_{gn}(s)}{Z_{1,a}(s)} = \frac{V_{ag}(s)}{Z_{1,a}(s)} \tag{18}$$

$$I_{1,b}(s) = \frac{V_{bn}(s) - V_{gn}(s)}{Z_{1,b}(s)} = \frac{V_{bg}(s)}{Z_{1,b}(s)} \tag{19}$$

$$I_{1,c}(s) = \frac{V_{cn}(s) - V_{gn}(s)}{Z_{1,c}(s)} = \frac{V_{cg}(s)}{Z_{1,c}(s)} \tag{20}$$

The voltage drops $V_{an}(s) - V_{gn}(s)$, $V_{bn}(s) - V_{gn}(s)$, and $V_{cn}(s) - V_{gn}(s)$ across the coupling impedances correspond to the phase-to-ground voltages $V_{ag}(s)$, $V_{bg}(s)$, and $V_{cg}(s)$, respectively. Combining (17)-(20) from M TIA channels and substituting admittances, i.e $Y(s) = 1/Z(s)$, yields

$$G_{tia}(s)\begin{bmatrix} Y_{1,a}(s) & Y_{1,b}(s) & Y_{1,c}(s) \\ Y_{2,a}(s) & Y_{2,b}(s) & Y_{2,c}(s) \\ \vdots & \vdots & \vdots \\ Y_{M,a}(s) & Y_{M,b}(s) & Y_{M,c}(s) \end{bmatrix}\begin{bmatrix} V_{ag}(s) \\ V_{bg}(s) \\ V_{cg}(s) \end{bmatrix} = \begin{bmatrix} V_{out,1}(s) \\ V_{out,2}(s) \\ \vdots \\ V_{out,M}(s) \end{bmatrix} \tag{21}$$

Purely capacitive coupling and rearranging terms turns (21) into

$$G_{tia}(s)\begin{bmatrix} C_{1,a} & C_{1,b} & C_{1,c} \\ C_{2,a} & C_{2,b} & C_{2,c} \\ \vdots & \vdots & \vdots \\ C_{M,a} & C_{M,b} & C_{M,c} \end{bmatrix}\begin{bmatrix} V_{ag}(s) \\ V_{bg}(s) \\ V_{cg}(s) \end{bmatrix} = \frac{1}{s}\begin{bmatrix} V_{out,1}(s) \\ V_{out,2}(s) \\ \vdots \\ V_{out,M}(s) \end{bmatrix} \tag{22}$$

With at least three measured channels and a full column rank matrix, sensor signal processing [9] uses TIA output measurements to produce sample-by-sample estimates of the voltage source vector of (22) in the discrete time domain,

$$\hat{\boldsymbol{v}}[n] = \begin{bmatrix} \hat{v}_{ag}[n] \\ \hat{v}_{bg}[n] \\ \hat{v}_{cg}[n] \end{bmatrix} = \begin{bmatrix} \hat{v}_{an}[n] - \hat{v}_{gn}[n] \\ \hat{v}_{bn}[n] - \hat{v}_{gn}[n] \\ \hat{v}_{cn}[n] - \hat{v}_{gn}[n] \end{bmatrix} \tag{23}$$

where "hatted" variables represent an estimate and n is the sample index of the digitized voltage signals. Stated another way, the voltage sensor estimates the potential of the cable wires with respect to the PE ground. In solidly grounded systems, $v_{gn}(t) \approx 0$ and

$$[\hat{v}_{ag}[n], \hat{v}_{bg}[n], \hat{v}_{cg}[n]]^{\mathrm{T}} \approx [\hat{v}_{an}[n], \hat{v}_{bn}[n], \hat{v}_{cn}[n]]^{\mathrm{T}} \tag{24}$$

For this case, phase-to-neutral voltages are the same as phase-to-ground voltages. The estimated phase-to-ground voltages from TIA output signal processing approximate the phase-to-neutral voltages. However, in ungrounded systems, there is no neutral wire and $V_{gn}(s)$ may be nonzero. In these grids, phase-to-phase voltages are of interest. Regardless of $V_{gn}(s)$, the noncontact voltage sensor can estimate line-to-line voltages through subtraction of the elements in $\hat{\boldsymbol{v}}[n]$. Written in matrix form

$$\begin{bmatrix} \hat{v}_{ab}[n] \\ \hat{v}_{bc}[n] \\ \hat{v}_{ca}[n] \end{bmatrix} = \begin{bmatrix} 1 & -1 & 0 \\ 0 & 1 & -1 \\ -1 & 0 & 1 \end{bmatrix}\begin{bmatrix} \hat{v}_{ag}[n] \\ \hat{v}_{bg}[n] \\ \hat{v}_{cg}[n] \end{bmatrix}. \tag{25}$$

An advantageous cancellation of the ground-to-neutral voltage occurs, to demonstrate, expanding operations in the first row yields

$$\begin{aligned} \hat{v}_{ab}[n] &= \hat{v}_{ag}[n] - \hat{v}_{bg}[n] \\ &= (\hat{v}_{an}[n] - \hat{v}_{gn}[n]) - (\hat{v}_{bn}[n] - \hat{v}_{gn}[n]) \\ &= \hat{v}_{an}[n] - \hat{v}_{bn}[n]. \end{aligned} \tag{26}$$

Similar expressions apply for $\hat{v}_{bc}[n]$ and $\hat{v}_{ca}[n]$.

The above analysis explicitly validates circuit techniques from [9] for a wide class of industrially relevant grid topologies. Equations (16)-(26) show that voltage reconstruction works provided that the capacitance matrix in (22) has linearly independent columns. Each column corresponds to the set of M capacitances from the sensing electrodes to one of the phase conductors. Because each phase conductor occupies a distinct area inside the cable, full column rank is practically guaranteed via cable and probe geometry. Also, for a typical power-monitoring sensor installation, the phase conductors will be large relative to the sensing electrodes. The distinct "view" or coupling capacitances to the wires from each electrode will manifest as varied structures of the columns. In summary, for situations well-modeled by Fig. 7, a calibrated array-based noncontact voltage sensor can faithfully reconstruct line-to-ground and line-to-line voltages. Importantly, reconstruction works regardless of the value of ground-to-neutral voltage V_{gn} or system impedances Z_{gn}, Z_{ag}, Z_{bg}, or Z_{cg}.

IV. EXPERIMENTAL VALIDATION

These sections provide experimental validation of the circuit analysis in Section III. Section IV-A describes the experimental hardware. Section IV-B presents characterization of the coupling capacitances for the specific sensor installation. Section IV-C presents reference-signal measurements in an ungrounded grid situation with different grounding impedances. Section IV-D presents voltage reconstruction results in an ungrounded grid scenario.

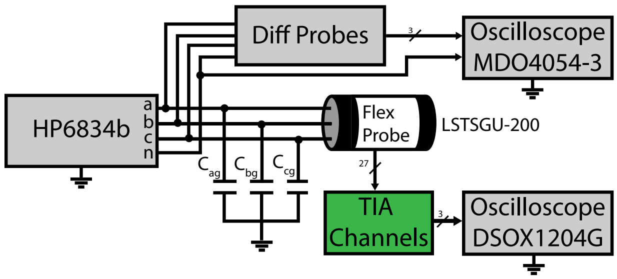

FIGURE 10. Block diagram of the experimental setup.

A. EXPERIMENTAL SETUP

Figure 10 shows a block diagram of the experimental setup for sensor model validation. An HP6834b three-phase power source drove the LSTSGU-200 three-wire shipboard power cable with a balanced set of ac three-phase voltages. The chassis' of all power equipment were bonded to PE ground. Terminal blocks provided connections from each phase and the source neutral point to PE ground. For example, in many tests, two $1\mu\text{F}$ film capacitors in series were connected from each phase to the PE ground. These capacitors were upstream of the LSTSGU-200 and near the output of the HP6834b. This series combination created $Z_{ag}(s) \approx Z_{bg}(s) \approx Z_{cg}(s) \approx 1/(s(0.5\mu\text{F}))$ and provided the flexibility to increase the phase-to-ground capacitance to $1\mu\text{F}$ on any phase by shorting out one of the series capacitors with a jumper wire. The output filter of the HP6834b also contributed to the phase-to-ground and neutral-to-ground impedance of the setup. This setup emulates of a variety of power system grounding scenarios. Capacitance measurements across the output terminals revealed about 1nF of capacitance across every output terminal (phase a, b, c, and neutral) to ground. A Tektronix MDO4054-3 oscilloscope measured the power supply phase-to-neutral voltages via differential probes and the neutral-to-ground voltage via a normal 10x oscilloscope probe. These "contact" measurements with the differential probes provide a "ground truth" for sensor voltage reconstruction performance. A Keysight DSOX1204G measured the outputs of the three multiplexed TIA channels. The SVDR supply setup of Fig. 4 powered the TIA board.

B. COUPLING CAPACITANCE CHARACTERIZATION

First, the electrode-to-wire capacitances for the sensor installation were characterized. The HP6834b was disconnected and the phase wires were shorted together. The Agilent 33210A excited the system with a 2.5 V amplitude, 800 Hz sinusoidal reference signal and the analog multiplexers cycled each TIA channel through their possible electrode connections. For each case, the DSOX1204G measured the rms voltage magnitude of the TIA output at 800 Hz. The expression

$$C_{sum,k} = \frac{|V_{out,k}(j\omega_{ref})|}{\omega_{ref}|G_{tia}(j\omega_{ref})||V_{ref}(j\omega_{ref})|} \tag{27}$$

with numerator equal to oscilloscope rms readings, $\omega_{ref} = 2\pi 800$ rad/sec, $|G_{tia}(j2\pi 800)| \approx 21.78\ \text{M}\Omega$, and $|V_{ref}(j2\pi 800)| = 2.5/\sqrt{2}$ Vrms generated capacitance estimates for each electrode index $k = [1, \ldots, 26]$. Fig. 11a plots $C_{sum,k}$ estimates versus electrode index. Index 1 started on the top side of the probe gap from the perspective in Fig. 1 and increased around the cable circumference until the sensing electrode just below the gap. The capacitance curve contains three distinct peaks and valleys, localizing the sensing electrodes with respect to the three internal wires. Larger values of $C_{sum,k}$ correspond to sensing electrodes positioned close to one cable wire and smaller values of

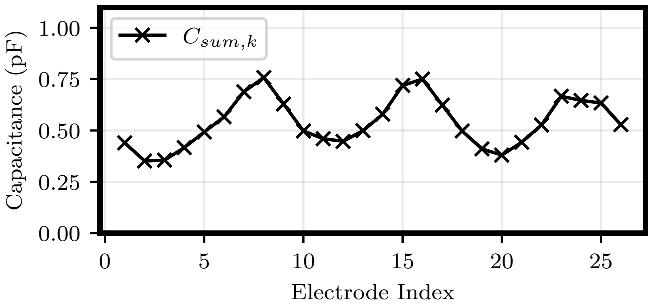

(a) C_{sum} estimates from 800 Hz reference signal excitation.

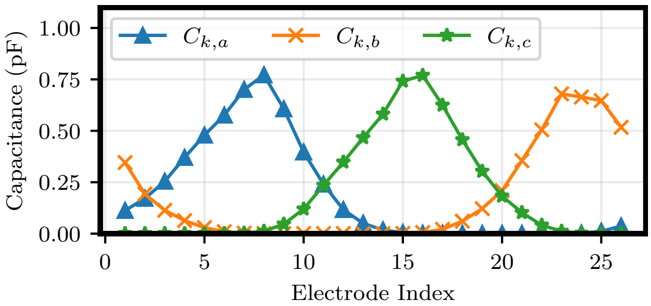

(b) $C_{k,\phi}$ estimates from single-phase 60 Hz grid voltage excitation. Each curve forms a column of the capacitance matrix in (22) for this sensor installation.

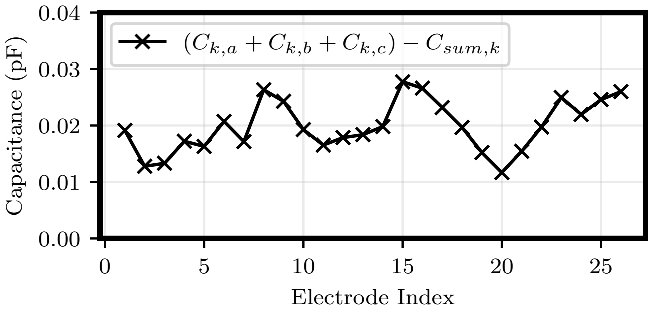

(c) Differences between the sum of capacitance estimates form single-phase 60 Hz grid excitation and capacitance estimates at 800 Hz from reference-signal excitation.

FIGURE 11. Coupling capacitance characterization with reference signal excitation and single-phase grid voltage 60 Hz excitation.

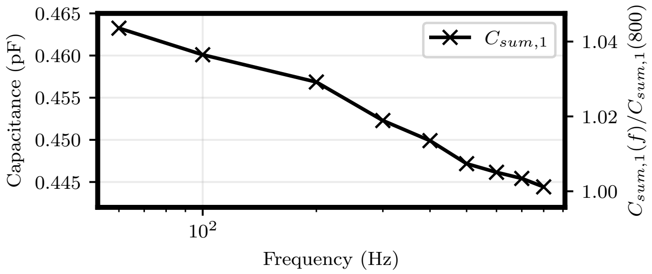

FIGURE 12. $C_{sum,1}$ **estimate versus reference signal frequency.**

$C_{sum,k}$ correspond to sensing electrodes positioned between two cable wires. This is the "image" of the cable seen by the sensor upon installation and the data which informs individual coupling capacitance estimation techniques [9].

Single-phase tests with the HP6834b validated reference signal measurements and investigated the individual coupling capacitances that comprise $C_{sum,k}$. The supply individually excited each phase wire with 120 Vrms, 60 Hz voltage and grounded the other two phase wires. A jumper wire bonded the source neutral and ground so the system was solidly grounded and $Z_{gn} \approx 0$. Note that this single phase excitation method is not practical for field installations and serves only to verify measurements and provide extra context for laboratory setups with controllable ac power sources. For each excited phase, the multiplexers cycled through the electrode connections and the DSOX1204G measured the ac rms voltage magnitude of the TIA output at 60 Hz. The expression

$$C_{sum,k} = \frac{|V_{out,k}(j\omega_{grid})|}{\omega_{grid}|G_{tia}(j\omega_{grid})||V_{\phi n}(j\omega_{grid})|} \tag{28}$$

with $\omega_{grid} = 2\pi 60$ rad/sec, $|G_{tia}(j2\pi 60)| \approx 21.80$ MΩ, and $|V_{\phi n}(j2\pi 60)| = 120$ Vrms for each excited phase ϕ generated capacitance estimates. Fig. 11b shows the resulting $C_{k,a}$, $C_{k,b}$, and $C_{k,c}$ estimates. Peaks and intersections of the individual capacitance curves in Fig. 11b match the peaks and valleys of Fig. 11a. For further comparison, Fig. 11c shows the difference between of the sum of the single-phase estimates from Fig. 11b for each index k and the $C_{sum,k}$ measurements from the 800 Hz reference signal of Fig. 11a. All capacitance estimates at 60 Hz were about 0.02 pF or 4% larger than estimates at at 800 Hz due to frequency-dependent dielectric properties of the cable insulation and filler. There is also correlation with the magnitude of $C_{sum,k}$. The variations of Fig. 11c around its average value of about 0.02 pF align with the peaks and valleys of Fig. 11a. This appears due to the proportion of different materials seen by electric flux paths for each sensing electrode. For example, the dominant flux path for an electrode directly over a cable wire is mostly through the cable outer jacket material. Whereas, the dominant flux path for an electrode centered between two wires may pass through more filler than outer jacket material. Each material may have slightly different permittivity variations with frequency.

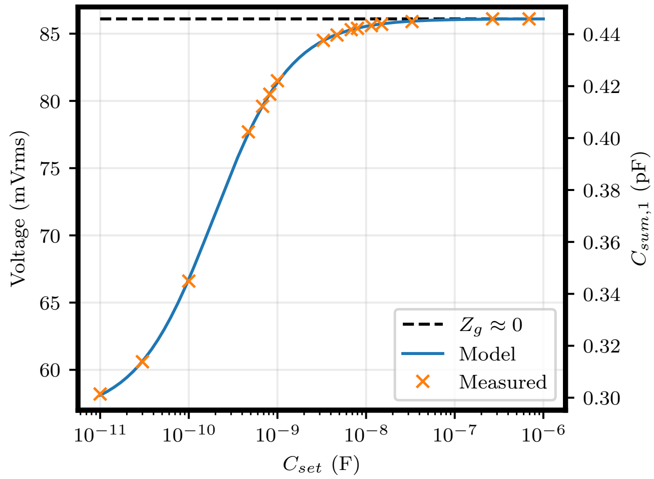

FIGURE 13. Comparison between circuit model preditions and reference signal measurements from TIA channel 1 for varied Z_g

.

A sensor in the field would characterize the frequency-dependent nature of coupling capacitance with different reference-signal frequencies. To demonstrate, Fig. 12 shows $C_{sum,1}$ estimates at 9 reference frequencies in the range [60, 800] Hz. Plotted with a logarithmic frequency axis, the capacitance decreases approximately linearly. For this data, a curve fit determines the necessary compensation to best approximate the capacitance value at frequencies of interest, e.g., 60 Hz and its odd harmonics. The secondary y axis on the right of Fig. 12 confirms the capacitance at 60 Hz is about 1.04 times larger than the capacitance at 800 Hz. Note, in an application scenario, reference frequencies would need to be carefully chosen to avoid overlap in spectral content from grid sources. Overall, with appropriate scaling, the $C_{sum,k}$ estimates from the sensor prototype tracked "benchmark" $C_{1,a}$, $C_{1,b}$, and $C_{1,c}$ values from single-phase tests.

C. REFERENCE SIGNAL TESTS

This section presents sensor reference signal measurements from an ungrounded power system with varying Z_g. The Agilent 33210A excited the system with a 2.5 V amplitude, 800 Hz sinusoidal reference signal. The HP6834b was disconnected and the phase wires were shorted together. Different capacitances were connected between the phase wires and the PE ground. This capacitance, called C_{set}, and the stray phases-to-ground capacitance of the experimental setup, called $C_{\phi g}$, determined Z_g. The DSOX1204G measured the output of TIA channel 1 for each value of Z_g. The TIA input was connected to sensing electrode 1 of Fig. 11a through the multiplexer.

Fig. 13 shows measurement results compared with circuit model calculations. The orange 'x' data markers represent TIA output magnitude measurements in mVrms from the DSOX1204G. The black dashed line extends the measured result of $|V_{out,1}(j2\pi 800)| = 86.1$ mV with $Z_g \approx 0$ for comparison. The solid blue line represents circuit model predictions

This article has been accepted for publication in IEEE Access. This is the author's version which has not been fully edited and
content may change prior to final publication. Citation information: DOI 10.1109/ACCESS.2026.3730400

and plots (13) scaled by $G_{tia}(j2\pi 800) \approx 21.80\ \mathrm{M\Omega}$. The second y axis label on the right shows the corresponding $C_{sum,1}$ estimate from $|v_{out,1}(j\omega_{ref})|/(|G_{tia}j\omega_{ref}||v_{ref}(j\omega_{ref})|)$. The model depends on two uncertain parameters of the setup that are not set by sensor design, C_o and $C_{\phi g}$. Tests with capacitance meters provided ballpark estimates and a parameter fit which minimized the squared error between model and measured results established their final values. For Fig. 13, the impedances were $Z_{coup}(s) = 1/(s(C_{sum} + C_o))$ with $C_{sum} = 0.445$ pF, $C_o = 65.1$ pF and $Z_g = 1/(s(C_{set} + C_{\phi g}))$ with $C_{\phi g} = 126.1$ pF.

The model aligns well with experimental measurements and verifies the analysis in Section III-B. Fig. 13 is effectively a visual representation of (15). As C_{set} increased and Z_g decreased, the TIA output approached the $Z_g \approx 0$ asymptote. For this TIA channel, (15) holds for approximately $C_{set} > 6.8$ nF. Below 6.8 nF, Z_g attenuates $|V_{out,1}(j\omega_{ref})|$ by more than 1% and the measured values deviate from 86.1 mV, leading to capacitance underestimate.

D. VOLTAGE RECONSTRUCTION

This section presents experimental voltage reconstruction results from the ungrounded power system setup of Section IV-A. These tests verify the analysis of Section III-C, specifically, equations (23)-(26). The measurements from Fig. 11a determined the electrode choices for voltage reconstruction tests. The prototype implemented the "Pick the Peaks" voltage reconstruction method from [9]. This method chooses the electrodes closest and most centered over a phase wire. These electrodes have large coupling to a single phase and nearly equal but small coupling to other phases, making the capacitance matrix in (22) approximately diagonal. Digitally scaled and integrated versions of measurements from their TIAs form system voltage estimates. For this installation, sensor hardware measured and processed signals from electrodes 8, 16, and 24.

Figures 14 and 15 display power system waveforms and noncontact voltage sensor estimates for tests with common system voltage conditions but balanced and unbalanced phase-to-ground capacitances, respectively. Figure 14a shows the phase-to-neutral and ground-to-neutral contact voltage measurements for the first test with 0.5 µF of external capacitance to ground per phase ($C_{ag} = C_{bg} = C_{cg} \approx 0.5$ µF). No capacitance was added between neutral and ground so $C_{gn} \approx 1$ nF from the output filter. The phase to neutral voltages were a balanced three-phase set and $v_{gn}(t) \approx 0$ due to the the balanced conditions. Note, as per (8), both balanced system voltages and balanced phase-to-ground impedances are required for $v_{gn}(t) = 0$. Figure 14b shows the phase-to-ground voltage estimates from the noncontact sensor compared to the contact phase-to-neutral voltage measurements. In this test, the phase-to-ground sensor estimates tracked the phase-to-neutral voltages similar to a well-calibrated sensor applied to a solidly grounded system. Figure 14c shows the phase-to-phase voltage estimates from the noncontact sensor compared to the contact phase-to-phase voltage measurements. Subtraction of the signals in Figure 14c computed these curves. Again, the phase-to-phase noncontact estimates tracked the phase-to-phase contact measurements.

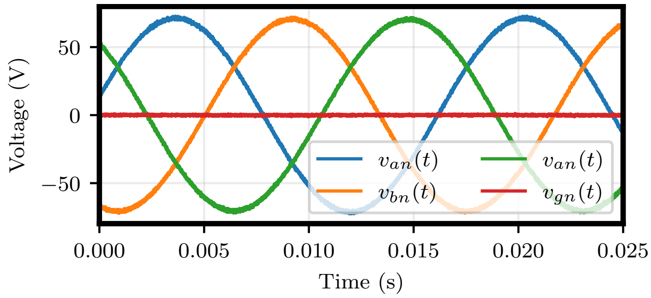

(a) Contact power supply measurements

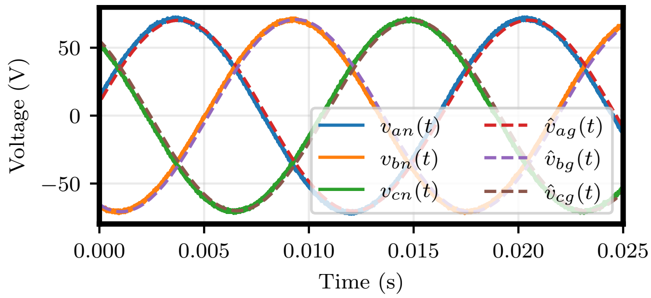

(b) Contact phase-to-neutral measurements and noncontact sensor estimates

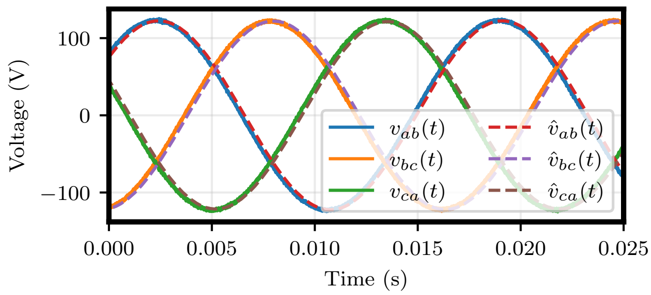

(c) Contact phase-to-phase measurements and noncontact sensor estimates

FIGURE 14. Measurements and noncontact sensor estimates for voltage reconstruction tests for balanced 0.5 µF phase-to-ground capacitances and $v_{gn}(t) \approx 0$.

Figure 15a shows the measured phase-to-neutral and ground-to-neutral contact voltage measurements from the same setup but with unbalanced external phase-to-ground capacitance ($C_{ag} \approx 1$µF, $C_{bg} = C_{cg} \approx 0.5$µF). The phase-to-neutral voltages were still a balanced three-phase set, but due to the imbalanced phase-to-ground impedances, $v_{gn}(t) \neq 0$ and varied sinusoidally. Figure 15b shows the phase-to-ground voltage estimates from the noncontact sensor compared to the contact phase-to-neutral voltage measurements. In contrast to Fig. 14b, the sensor phase-to-ground estimates in Fig. 15b did not track the phase-to-neutral measurements. The phase-to-ground estimates differ predictably by $v_{gn}(t)$ in agreement with (23). The dashed lines are correspondingly higher or lower than the solid lines by the amount of $v_{gn}(t)$ in Fig. 15a. Despite the discrepancy in the phase-to-neutral measurements and phase-to-ground estimates, Figure 15c

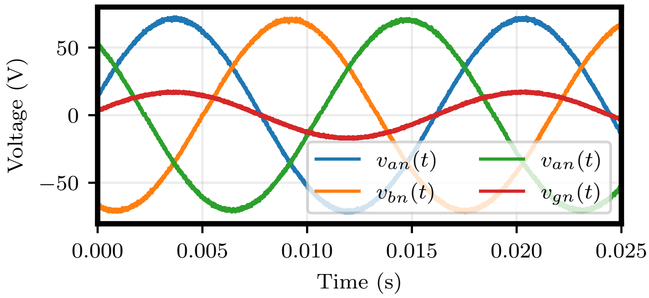

(a) Contact power supply measurements

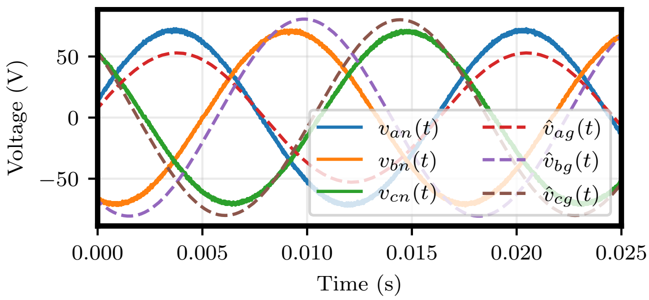

(b) Contact phase-to-neutral measurements and noncontact sensor estimates

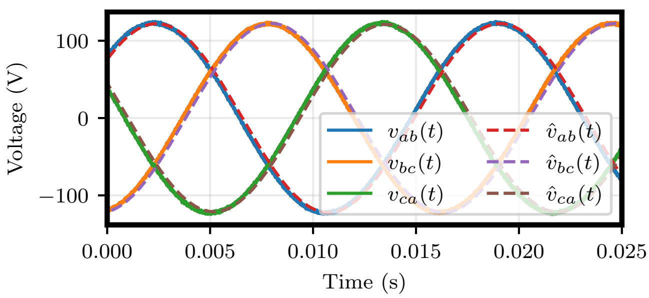

(c) Contact phase-to-phase measurements and noncontact sensor estimates

FIGURE 15. Measurements and sensor estimates for voltage reconstruction tests for unbalanced phase-to-ground capacitances ($C_{ag} \approx 1\ \mu\text{F}$, $C_{bg} = C_{cg} \approx 0.5\mu\text{F}$) and $v_{gn}(t) \neq 0$.

demonstrates correct phase-to-phase voltage reconstruction. Through the cancellation explained in (25) and (26), the noncontact voltage sensor phase-to-phase estimates tracked the phase-to-phase voltage measurements.

V. CONCLUSION

This article extends capacitive noncontact three-phase voltage sensing analysis beyond solidly-grounded power systems. Key takeaways include: first, for reliable use on all grids, measurement circuitry should be referenced with respect to protective earth (PE) ground. Second, accurate capacitance estimation with the injected reference signal requires system grounding impedances to be small relative to the sensor coupling impedances. Third, given a full-column rank coupling capacitance matrix, a capacitive noncontact sensor can reconstruct line-to-ground and line-to-line grid voltage waveforms regardless of system grounding strategy.

The modeling, analysis, and hardware presented in this paper enable a variety of new developments for noncontact power monitoring. First, a power meter requires current sensing. An array of magnetic field sensors could work in tandem with the noncontact voltage sensing electrode array. Next, a deployable and field-ready sensor package requires further minimization compared to existing prototypes. Enabled by the multiplexed transimpedance amplifier (TIA) board design from Section II, future sensor iterations could combine the sensing electrodes and TIA circuits into a rigid-flex structure. Finally, potential installations may occupy harsh environments with significant electromagnetic interference (EMI) and use power cables with a variety of geometries. Specific tests with nearby interfering sources could characterize and validate the shielding practices of the existing sensor probe. Similarly, tests with different power cables can confirm existing designs and perhaps motivate new electrode configurations.

REFERENCES

[1] Esdras Battosti Da Silva, Hiago Galindo De Almeida, Gabriel De Abreu Silva, Ruhan Pontes Policarpo De Souza, Cristiano Marcos Agulhari, Marcelo Favoretto Castoldi, Alessandro Goedtel, and Wesley Angelino De Souza. Non-intrusive load monitoring (nilm): A systematic review of observability regimes, methods, and evaluation paradigms. *IEEE Access*, 14:29418–29455, 2026.

[2] Qi Zhu, Guangchao Geng, and Quanyuan Jiang. Contactless wideband current measurement based on tunneling magnetoresistance sensor array for rectangular busbar systems. *IEEE Transactions on Instrumentation and Measurement*, 74:1–11, 2025.

[3] Sungjun Yoon, Tanwei Yan, and Jose Silva-Martinez. High-resolution battery-less miniaturized power grid monitoring system employing a capacitive sensing current-mode $\sigma\delta$ modulator. *IEEE Transactions on Instrumentation and Measurement*, 74:1–12, 2025.

[4] S. Prakash, V. Saikumar, Anjan Chakaravorty, Amitava DasGupta, Deleep R. Nair, and Boby George. Self-powered, non-intrusive electric power monitoring system for home: A feasibility study. *IEEE Sensors Journal*, pages 1–1, 2025.

[5] Abdelhay A. Sallam and Om P. Malik. *Electric Distribution Systems*. Wiley-IEEE Press, Piscataway, NJ, 2019.

[6] Mohammed M. Islam. *Shipboard Power Systems Design and Verification Fundamentals*. Wiley-IEEE Standards Association, Piscataway, NJ, 2018.

[7] Mohammed M. Islam. *VFD Challenges for Shipboard Electrical Power System Design*. Wiley-IEEE Standards Association, Piscataway, NJ, 2020.

[8] Norbert Doerry, Mohammed M. Islam, and John Prousalidis. *Design of Shipboard Power System Grounding / Earthing*. Wiley-IEEEPress, Piscataway, NJ, 2025.

[9] Thomas C. Krause and Steven B. Leeb. Voltage measurement of multiwire cables with a noncontact electrode-array sensor. *IEEE Transactions on Instrumentation and Measurement*, pages 1–1, 2025.

[10] Dongping Xiao, Tao He, Wenhan Zhao, Xuefei Du, and Yutong Xie. Improved three-dimension mathematical model for voltage inversion of ac overhead transmission lines. *IEEE Access*, 7:166740–166748, 2019.

[11] Fani Barakou, Peter A. A. F. Wouters, Shima Mousavi-Gargari, Jan P. W de Jong, and E. Fred Steennis. Online transient measurements of ehv cable system and model validation. *IEEE Transactions on Power Delivery*, 34(2):532–541, 2019.

[12] Peter Wouters, Armand van Deursen, and Mischa Vermeer. Methodology and accuracy for non-invasive detection of switching transient overvoltages from compensation coils connected to power transformers. *IET Science, Measurement & Technology*, 14(2):173–181, 2020.

[13] M. A. Haberman and E. M. Spinelli. Noncontact ac voltage measurements: Error and noise analysis. *IEEE Transactions on Instrumentation and Measurement*, 67(8):1946–1953, 2018.

[14] Marcelo Alejandro Haberman, Enrique Mario Spinelli, and Ferran Reverter. A supply-voltage driving scheme for grounded capacitive sensor front-ends. *IEEE Transactions on Instrumentation and Measurement*, 71:1–7, 2022.

[15] Marcelo Alejandro Haberman and Enrique Mario Spinelli. An analog front-end circuit for noncontact voltage measurements, immune to input

capacitance. *IEEE Transactions on Instrumentation and Measurement*, 74:1–8, 2025.

[16] J. Millman. A useful network theorem. *Proceedings of the IRE*, 28(9):413–417, 1940.

[17] J O Flower. Unbalanced three-phase electrical network calculations, with particular reference to fault-conditions, via the millman theorem. *Journal of Marine Engineering & Technology*, 2(1):36–42, 2003.

[18] Simon Lee Grace. A millman based alternate to symmetric component methods for fault level calculations in marine power systems. *Journal of Marine Engineering & Technology*, 21(1):38–53, 2022.

[19] John Prousalidis. Analysis of unbalanced fault operating conditions of ship electric networks via millman's theorem. *Journal of Marine Engineering & Technology*, 21(6):324–333, 2022.

THOMAS C. KRAUSE (Member, IEEE) received the B.S. degree in electrical engineering from Purdue University, West Lafayette, IN, USA, in 2019, and the M.S., E.E., and Ph.D. degrees in electrical engineering and computer science from the Massachusetts Institute of Technology, Cambridge, MA, USA, in 2021, 2024, and 2026 respectively. He is currently an Assistant Professor in the Elmore Family School of Electrical and Computer Engineering at Purdue University.

AARON W. LANGHAM (Member, IEEE) received the B.E.E. degree in electrical engineering from Auburn University, Auburn, AL, USA in 2018, and the M.S., E.E., and Ph.D. degrees in electrical engineering and computer science from the Massachusetts Institute of Technology, Cambridge, MA, USA in 2022, 2024, and 2026, respectively. He is currently an Assistant Professor at The Cooper Union for the Advancement of Science and Art in New York, NY. His research interests include signal processing, machine learning, and IoT platforms for energy systems.

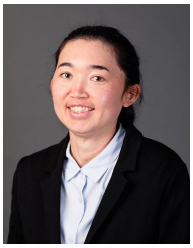

DAISY H. GREEN (Senior Member, IEEE) received the B.S. degree in electrical engineering from the University of Hawai‘i at Mānoa, Honolulu, HI, USA, in 2015, and the M.S. degree and the Ph.D. degree in electrical engineering and computer science from the Massachusetts Institute of Technology, Cambridge, MA, USA, in 2018 and 2022, respectively. She is currently an Assistant Professor with the department of electrical and computer engineering at UH Mānoa. Her research interests include monitoring and control of electric energy systems.

STEVEN B. LEEB (Fellow, IEEE) received the Ph.D. degree from the Massachusetts Institute of Technology, in 1993. Since 1993, he has been a member on the MIT Faculty with the Department of Electrical Engineering and Computer Science. He also holds a joint appointment with the Department of Mechanical Engineering, MIT. He is concerned with the development of signal processing algorithms for energy and real-time control applications.